

Letter

Revisiting the age and emplacement process of the Huangshandong Ni–Cu deposit in the Central Asian Orogenic belt, northwestern China: Implications for multiple magma extractions from a short-lived staging magma chamber



Ya-Jing Mao ^{a,b,*}, Ke-Zhang Qin ^{a,b,c,*}, Dongmei Tang ^{a,b}

^a Key Laboratory of Mineral Resources, Institute of Geology and Geophysics, Chinese Academy of Sciences, Beijing 100029, China

^b Institutions of Earth Science, Chinese Academy of Sciences, Beijing 100029, China

^c University of Chinese Academy of Sciences, Beijing 100049, China

ARTICLE INFO

Article history:

Received 15 February 2018

Accepted 2 August 2018

Available online 7 August 2018

Keywords:

Central Asian Orogenic belt
Huangshandong Ni–Cu deposit
Mafic-ultramafic intrusion
Multiple magmatism
Staging magma chamber

ABSTRACT

Magmatic Ni–Cu deposits that associated with mafic-ultramafic intrusions in convergent settings could form from multiple magma pulses with age difference varying from 1 Ma to >10 Ma years. The Huangshandong deposit in NW China of the southern Central Asian Orogenic Belt was formed in such a setting. The intrusion is composed of four units formed by four magma pluses: a gabbroic sequence (Phase I, crystallized from an evolved magma), a sheet-like ultramafic body (Phase II, crystallized from a relatively primitive magma), a dike-like gabbronorite body (Phase III, crystallized from an evolved magma), and an irregular ultramafic unit (Phase IV, crystallized from a relatively primitive magma). Our zircon SIMS U–Pb dating shows that the Phase I and Phase IV magmas of the Huangshandong deposit were emplaced at 280.3 ± 1.9 Ma and 281.4 ± 2.2 Ma, respectively, indicating that the four magma pulses were intruded over a very short period and cannot be distinguished within the uncertainty of ± 2 Ma. Moreover, the zircon crystals in the four units record identical ϵHf (t) values (average of 12.1–13.5) and $\delta^{18}\text{O}$ values (average of 6.3–6.5‰). However, the intrusive relationships of the four units illustrate that the Huangshandong complex cannot form by in-situ fractionation. Therefore, the indistinguishable Hf–O isotopic values, together with their contemporaneous emplacements, indicate that the four magma pulses could originate from a same staging magma chamber. The overall enrichment of ϵHf (t) value relative to that of the depleted mantle (16) and elevation of $\delta^{18}\text{O}$ values relative to the mantle value (5.3‰) suggest 15–20% crustal material incorporation. Additionally, the magmas may have been contaminated prior to their arrival at the staging magma chamber, where the magma has subsequently experienced variable olivine fractionations and relatively primitive magma replenishment. For most mafic-ultramafic intrusions which are characterized by long-duration magmatism (>10 Ma) in convergent settings, e.g., intrusions in the Kalatongke area, Tulaergen intrusions, Xiarihamu intrusions, the most important Ni–Cu mineralization are closely related to the last stage magmatism. This finding suggests that the intrusions emplaced at the late stage of subduction and post-collisional period of the orogenic process may have more potential for Ni–Cu mineralization exploration.

© 2018 Elsevier B.V. All rights reserved.

1. Introduction

A single intrusion commonly crystallizes within 1 Ma, e.g. Cawthorn and Walraven (1998) have suggested that the ~2054 Ma Bushveld

complex (Scoates and Friedman, 2008), noted to be the world's largest layered intrusion, solidified within 75,000 years. However, recent studies on many small mafic-ultramafic intrusions in convergent settings (Lightfoot and Evans-Lamswood, 2015; Tang, 1996) illustrate that some of these intrusions crystallized from multiple magma pulses that could have had an age difference from several million years up to 100 Ma (Gehrels et al., 1987; Li et al., 2015; Saleeby, 1992; San et al., 2010; Su et al., 2014; Xue et al., 2016). Such magmas may have formed

* Corresponding author at: Key Laboratory of Mineral Resources, Institute of Geology and Geophysics, Chinese Academy of Sciences, Beijing 100029, China

E-mail addresses: maoyjing@mail.igcas.ac.cn (Y.-J. Mao), [\(K.-Z. Qin\).](mailto:kzq@mail.igcas.ac.cn)

during subduction and/or in post-collisional setting, and different pulses have variable potential of Ni–Cu sulfide mineralization. Thus, for mafic-ultramafic intrusions formed by multiple magma pulses, it is very important to address the age and origin of different magma pulses.

The Huangshandong complex, one of the four largest Ni–Cu deposits in the Central Asian Orogenic Belt (CAOB), is comprised of four units formed from four magma pulses, namely: gabbroic rocks (Phase I), ultramafic rocks (Phase II), gabbroic rocks (Phase III), ultramafic rocks (Phase IV) (Mao et al., 2015; Wang et al., 1987). Han et al. (2004) performed SHRIMP U–Pb dating on zircons separated from Phase I and yielded a concordant age of 274 ± 3 Ma. Despite subsequent intensive study of the Huangshandong complex (Deng et al., 2014; Gao and Zhou, 2013a; Han et al., 2004; Mao et al., 2015; Sun et al., 2013; Zhou et al., 2004), no age data exist for the other three phases, a gap, that should be filled to critically understand the evolutionary history of the Huangshandong complex.

In this contribution, the SIMS U–Pb dating of zircon crystals separated from Phase I and Phase IV rocks is conducted to further constrain the time evolution of the Huangshandong complex. In addition, the O–Hf isotopic compositions of the zircon grains from the four phases are used to better understand the magma evolution at the deep-seated magma chamber. The results from the Huangshandong complex, together with the evolution timeline of other mafic-ultramafic intrusions in convergent settings, are used to constrain the temporal control on the Ni–Cu mineralization in such setting. The findings improve our understanding of the Huangshandong Ni–Cu deposit and have several implications for the genesis of the Huangshandong deposit and exploration of Ni–Cu deposits in convergent settings.

1.1. Geological background

The Huangshandong complex is located in the East Tianshan (also known as Eastern Tianshan, Xiao et al., 2004) along the southern margin of the CAOB (Fig. 1a) and belongs to a cluster of Permian Ni–Cu sulfide-bearing mafic-ultramafic intrusions in NW China (Qin et al., 2011). The geological and geochemical characteristics of these deposits and the general geology of the East Tianshan have been detailed in several recent publications (Mao et al., 2018; Qin et al., 2011; Song et al., 2013). The Huangshandong complex is also among the four most important Ni–Cu deposits in the CAOB, together with the Huangshanxi, Kalatongke and Hongqiling deposits. The Huangshandong and Huangshanxi deposits belong to the Huangshan district, which also contains the Xiangshan deposit in the north and the Huangshannan deposit in the south (Fig. 1b). All of the deposits in the Huangshan district were emplaced along the Kangguer–Huangshan fault zone, and the distances between each of deposits are <30 km.

The lens-shaped Huangshandong complex hosts >50 Mt. of sulfide ores with average grades of 0.52 wt% Ni and 0.27 wt% Cu (Wang et al., 1987). The geological information of the Huangshandong complex was detailed in Wang et al. (1987) and Mao et al. (2015). In summary, the intrusion is composed of four rock units: a layered gabbroic sequence (Phase I), a sheet-like ultramafic body (Phase II), a dike-like gabbronorite body (Phase III) and an irregular ultramafic unit (Phase IV) (Fig. 1b–d). The layered gabbroic body consists of olivine gabbro, gabbro and hornblende gabbro at the center. Sulfide mineralization occurs in the upper portion of this unit, connecting with the basal sulfide mineralization in the Phase II rocks. These sulfides in Phase I are believed to have percolated from the Phase II magma (Mao et al., 2015). The Phase II rock, which is a sheet-like ultramafic body, exhibits an upwardly concave shape in cross-sectional view (Fig. 1d) and consists of olivine websterite and lherzolite. Disseminated and net-textured sulfides are present at the basal portion of this unit. The Phase III gabbronorite, which is a dike-like body, occurs to the west (Fig. 1c). The thickness of this injected dike-like body reaches ~ 200 m. Disseminated and net-textured ores mainly occur as small lenses in the center of the dike (Fig. 1c). Several small massive sulfide veins and semi-massive sulfide

patches are also present. The irregularly shaped Phase IV lherzolite and olivine websterite intersect the lower part of the layered gabbroic sequence (Phase I) and the dike-like gabbronorite body (Phase III). Disseminated and net-textured sulfides are present in various regions of this unit. Economic sulfide mineralization is hosted by rocks of the four magma pulses, whereas the most important orebodies are hosted by the Phase II to Phase IV rocks.

2. Analytical methods

Zircon grains from the Phase I olivine gabbro, Phase II olivine websterite, Phase III gabbronorite, and Phase IV olivine websterite were separated using standard density and magnetic separation techniques. These grains, alongside the zircon standards Penglai and Qinghu, were mounted in an epoxy resin. The mount was polished to expose the centers of the grains. All the zircon grains were documented with transmitted and reflected light micrographs and cathodoluminescence (CL) images to examine their internal structures. The CL imaging was performed on a LEO1450VP scanning electron microscope with a MinicL detector at the Institute of Geology and Geophysics, Chinese Academy of Sciences (IGGCAS).

Measurements of U, Th and Pb were conducted using the CAMECA IMS 1280 ion microprobe at the IGGCAS. The analytical protocols and procedures followed those in Li et al. (2010). The measured Pb isotopic compositions were corrected for common Pb using non-radiogenic ^{204}Pb . The corrections were acceptably small to be insensitive to the preference for a common Pb composition. An average of the present-day crustal composition (Stacey and Kramers, 1975) was used for the common Pb. The uncertainties of individual analyses were reported at a 1-sigma level; the mean ages for pooled U–Pb analyses are shown with a 95% confidence interval.

Subsequently, zircon O isotopes were measured by the CAMECA IMS 1280 ion microprobe on the same grain analyzed for U and Pb. The Cs + primary ion beam was accelerated at 10 kV with an intensity of ca. 2 nA and rastered over a 10 μm -area with a spot diameter of 20 μm . The internal precision of a single analysis was generally better than 0.2‰ for the $^{18}\text{O}/^{16}\text{O}$ ratio. The ^{18}O values were standardized to the Vienna Standard Mean Ocean Water (VSMOW) and reported in standard per mil (‰) notation. The instrumental mass fractionation factor was corrected by the Penglai zircon standard with $\delta^{18}\text{O}_{\text{VSMOW}} = 5.31\text{\textperthousand}$ (Li et al., 2010). The measured $^{18}\text{O}/^{16}\text{O}$ was normalized using VSMOW compositions and then corrected for the instrumental mass fractionation factor.

Finally, Lu–Hf isotopes were measured using laser-ablation multi-collector inductively coupled plasma mass spectrometry (LA-ICP-MS) on the same zircon grains that were previously analyzed for U–Pb and O isotopes. Lutetium–Hf isotopic analyses were obtained with ablation pits of 40–80 μm in diameter, an ablation time of 26 s and a repetition rate of 8 Hz. The measured $^{176}\text{Hf}/^{177}\text{Hf}$ ratios were normalized to $^{179}\text{Hf}/^{177}\text{Hf} = 0.7325$.

3. Results

3.1. Zircon U–Pb isotopes

Most of the zircons were fragments rather than intact crystals. The zircon fragments of the Phase I rocks were larger than those of the Phase IV rocks (Fig. 2a–b), probably due to their longer residence time in Zr-saturated liquid. In the CL images (Fig. 2a–b), most of the zircon fragments from both the Phase I and Phase IV rocks displayed oscillatory or sector zoning, whereas some of the zircons were too dark to show textural information under the analytical conditions in this study. The darker zircon grains had slightly higher U and Th concentrations than those in lighter grains (Table 1). The U and Th concentrations of lighter zircon from Phase I olivine gabbro varied from 194 to 388 ppm and from 43 to 147 ppm, respectively, whereas those of the darker zircon from

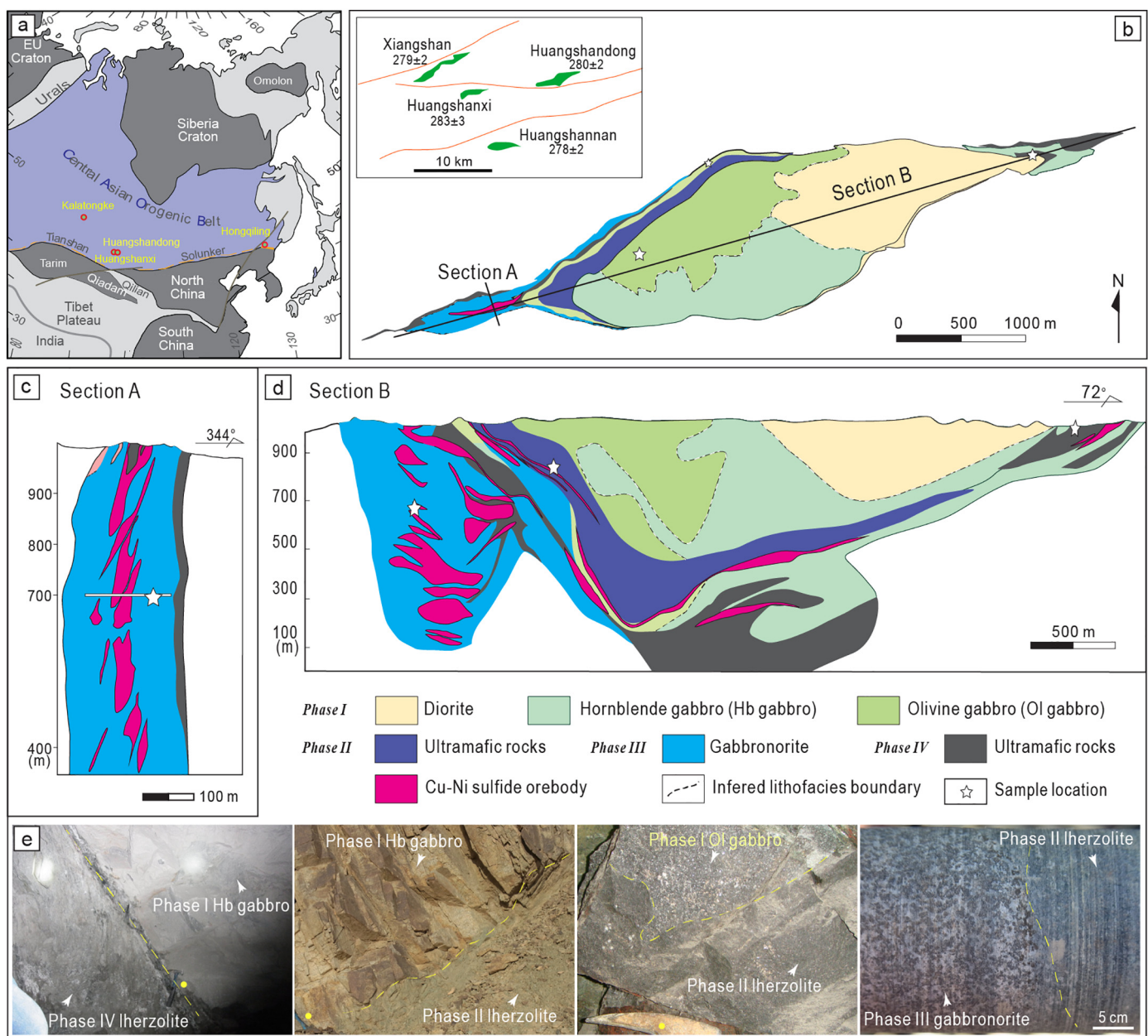


Fig. 1. Simplified geological map of the Central Asian Orogenic belt (a), a simplified geological map (b), cross sections (c, d), and field pictures (e) of the Huangshandong mafic-ultramafic complex (after Mao et al., 2015). The yellow dot in f shows the location of a hammer. The yellow dashed line shows the intrusive contact between rocks from the different phases.

Phase I varied from 600 to 1293 ppm and from 236 to 889 ppm, respectively. However, the darker zircon crystals from Phase I yielded $^{206}\text{Pb}/^{238}\text{U}$ ages similar to those of the lighter zircon crystals (Table 1), suggesting that all the zircon crystals crystallized from the same magma. The U and Th concentrations in zircon from Phase IV olivine websterite, which varied from 215 to 1406 ppm and from 96 to 1491 ppm, respectively, were slightly higher than those in the Phase I zircons. The Phase I zircon yielded a concordant age of 280.3 ± 1.9 Ma (Fig. 2c) with a mean standard weighted deviation (MSWD) of 1.6 (95% confidence), whereas the Phase IV zircon yielded a concordant age of 281.4 ± 2.2 Ma (Fig. 2c) with a MSWD of 0.43 (95% confidence). The ages of the Phases I and IV rocks showed that all four phases of the Huangshandong complex were emplaced at ~281 Ma and solidified over a very short period of time. The concordant age of ~280 Ma for the two units of the intrusion could rule out the possibility that the zircons were incorporated from the wall rock which formed at the

Carboniferous. Thus, the Hf and O isotopes in zircon crystals from the different rocks, as discussed in detail below, most likely recorded the signature of the magma during crystallization. Moreover, the new SIMS age of the Huangshandong complex is consistent with the emplacement age (~280 Ma, Figs. 1, 3) of the Ni–Cu deposits in the Huangshan district.

3.2. Zircon O–Hf isotopes

The ϵHf (t) and $\delta^{18}\text{O}$ values of zircons from Phase I olivine gabbro varied from 10.4 to 15.0 (with an average of 13.0), and from 6.0‰ to 6.7‰ (with an average of 6.4‰), respectively (Table 2). The average ϵHf (t) values of zircons from Phase II olivine websterite, Phase III gabbronorite, and Phase IV olivine websterite were 13.5, 12.9, and 12.1, respectively, whereas the corresponding $\delta^{18}\text{O}$ values were 6.3‰, 6.4‰, and 6.3‰, respectively. All the results of zircon analyzed from

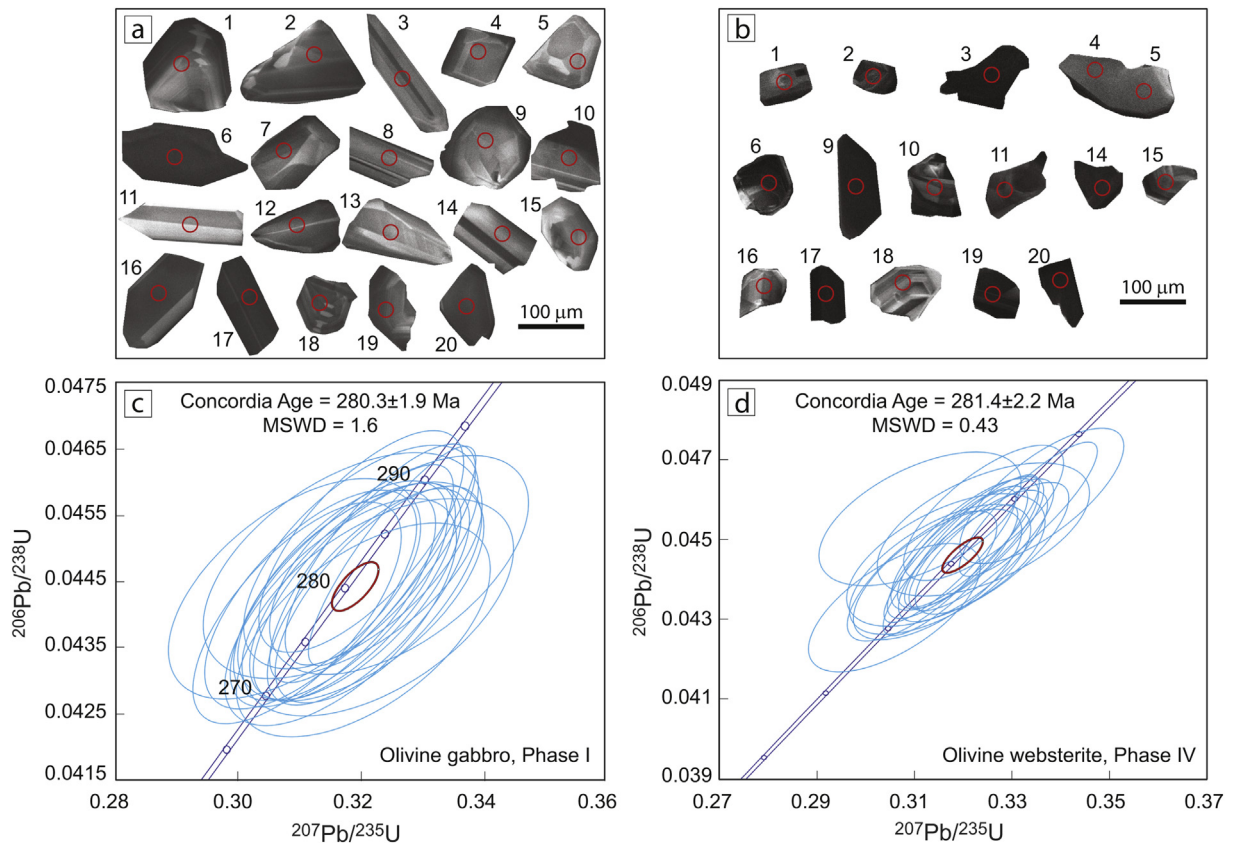


Fig. 2. The CL images and concordant ages of the zircon crystals separated from the Phase I (a, c) and Phase IV (b, d) rocks from the Huangshandong complex.

the four rock phases were comparable in terms of the O–Hf isotopic values (Fig. 4). The average zircon ϵ_{Hf} (t) values (12.7) of the Huangshandong complex in this study were slightly lower than the results from Sun et al. (2013, average value of 15.2), but were generally comparable to those of other intrusions in the Huangshan district, such as the Huangshanxi intrusion (ϵ_{Hf} (t) = 12.0, Su et al., 2011), Huangshannan intrusion (ϵ_{Hf} (t) = 13.1, Mao et al., 2016), and Xiangshan Ni–Cu associated gabbro (ϵ_{Hf} (t) = 12.9, Su et al., 2011). In addition, the slightly elevated $\delta^{18}\text{O}$ values (~6.3‰) of zircons from the Huangshandong complex were identical to those from the Huangshannan intrusion (~6.5‰, Mao et al., 2016) and Huangshanxi intrusion (6.1‰, Su et al., 2011) but higher than those from the Xiangshan Ni–Cu associated gabbro (4.9‰, Su et al., 2011). Based on the assumption that the SiO₂ content of melt is 53 wt% (Mao et al., 2015; Valley et al., 2005), the calculated $\delta^{18}\text{O}$ values for the melts of different magma pulses in equilibrium with the zircon crystals of the Huangshandong complex vary from 6.5‰ to 7.4‰ (average, 6.9‰).

4. Discussion

4.1. Evolution of the Huangshandong magmas in the deep-seated magma chamber

The spatial distribution and the intrusive relationship between the rocks from the different phases (Wang et al., 1987) showed that the Huangshandong complex could not have formed from in-situ fractionation and/or contamination processes in its current location. We assume the mantle derived melts have $\delta^{18}\text{O}$ values of 6.1‰ (Eiler et al., 2000) and ϵ_{Hf} (280) values of 16 (Vervoort and Blichert-Toft, 1999), and the average crust in the East Tianshan has $\delta^{18}\text{O}$ value of 10‰ and ϵ_{Hf} (280) value of 5 (Valley et al., 2005; Wang et al., 2008), the choice of the Hf–O isotopic composition of the East Tianshan crust is consistent with its juvenile arc crust nature and has been detailed in Mao et al.

(2016). According to the mixing modeling, such slightly enriched Hf–O isotopic values of the Huangshandong complex require approximately 10–25% crustal contamination (Fig. 4). It is important to note that 1σ uncertainty (0.2‰) of the $\delta^{18}\text{O}$ values could generate ~5% error of crustal contamination degree estimation. Thus, the relatively wide range of crustal contamination is likely derived from analytical uncertainty. Considering the analytical uncertainty, the more reasonable contamination degree of the magmas of the Huangshandong should be 15–20%. Nevertheless, the identical Hf–O isotopic values of the four magma pulses, together with the indistinguishable ages of Phases I and IV rocks, illustrates that these magmas may have extracted from the same staging magma chamber. Moreover, the contamination process probably occurred before the arrival of the magmas to the staging chamber, in which fractionation was the dominant factor according to the identical Hf–O isotopic values. Based on these restraints, we categorize four stages of the magma evolution process at the deep-seated staging magma chamber (Fig. 5), corresponding to the emplacement of the four magma phases in the current shallow location (Mao et al., 2015).

The first stage involved the ascent of the parental magma from the deep-seated staging chamber to a junction between the fault and weak planes (sub-chamber), where the magma experienced significant olivine fractionation (Fig. 5a), during which sulfide droplets probably accumulated to form disseminated–massive ore at the sub-chamber. The plumbing of this fractionated magma formed the Phase I evolved magma, which further ascended to the current chamber and crystallized into gabbroic rock. Meanwhile, minor olivine fractionation may have occurred at the bottom and boundaries of the staging magma chamber, accompanied by downward-settling of existing sulfide droplets and segregation of new sulfide droplets from the parental magma. The plumbing of the sulfide droplet-bearing parental magma through the current intrusion location formed the Phase II lherzolite and olivine websterite with disseminated sulfides (Fig. 5b). A proportion of sulfide

Table 1

Uranium, Th and Pb concentrations and U–Pb isotopes of zircons in Phase I and IV rocks from the Huangshandong complex.

Sample	U ppm	Th ppm	Pb ppm	Th/U	$^{207}\text{Pb}/^{235}\text{U}$	$\pm \sigma\%$	$^{206}\text{Pb}/^{238}\text{U}$	$\pm \sigma\%$	$^{207}\text{Pb}/^{206}\text{Pb}$	$\pm \sigma\%$	$^{206}\text{Pb}/^{238}\text{U}$	$\pm \sigma\%$
Phase I, olivine gabbro												
G2@01	284	109	15	0.383	0.31193	2.27	0.0442	1.52	0.05116	1.69	278.9	4.1
G2@02	340	91	17	0.269	0.32299	2.13	0.0443	1.50	0.05288	1.52	279.4	4.1
G2@03	290	110	15	0.380	0.32289	2.81	0.0441	1.51	0.05310	2.37	278.2	4.1
G2@04	303	112	16	0.370	0.30969	2.25	0.0440	1.55	0.05103	1.63	277.7	4.2
G2@05	217	43	11	0.199	0.32052	2.64	0.0438	1.50	0.05312	2.18	276.1	4.1
G2@06	843	417	45	0.495	0.32136	2.10	0.0443	1.50	0.05266	1.47	279.2	4.1
G2@07	285	101	15	0.356	0.30928	2.72	0.0444	1.52	0.05054	2.26	279.9	4.2
G2@08	348	138	18	0.396	0.32019	2.14	0.0451	1.51	0.05150	1.51	284.3	4.2
G2@09	272	106	14	0.388	0.31682	2.44	0.0440	1.58	0.05218	1.86	277.8	4.3
G2@10	379	147	20	0.388	0.31555	2.17	0.0442	1.50	0.05174	1.57	279.0	4.1
G2@11	224	85	12	0.380	0.32015	2.45	0.0449	1.53	0.05176	1.91	282.9	4.2
G2@12	328	120	17	0.366	0.31922	2.21	0.0443	1.50	0.05221	1.62	279.7	4.1
G2@13	194	76	10	0.393	0.32636	2.65	0.0447	1.50	0.05291	2.18	282.1	4.1
G2@14	205	79	11	0.385	0.32011	2.57	0.0443	1.52	0.05236	2.07	279.7	4.2
G2@15	305	109	16	0.357	0.31714	2.93	0.0447	1.55	0.05142	2.49	282.1	4.3
G2@16	600	236	31	0.392	0.32024	1.91	0.0446	1.50	0.05206	1.19	281.3	4.1
G2@17	1293	889	74	0.687	0.32523	1.72	0.0449	1.50	0.05256	0.84	283.0	4.2
G2@18	643	293	34	0.456	0.31680	2.26	0.0444	1.52	0.05181	1.67	279.7	4.2
G2@19	388	71	19	0.182	0.31906	2.12	0.0443	1.50	0.05219	1.49	279.7	4.1
G2@20	647	263	34	0.407	0.32331	1.97	0.0449	1.51	0.05223	1.26	283.1	4.2
Phase IV, olivine websterite												
HSD9@1	344	204	19	0.592	0.31527	2.41	0.0443	1.50	0.05167	1.89	279.1	4.1
HSD9@2	1356	1491	85	1.100	0.32181	1.75	0.0450	1.50	0.05191	0.90	283.5	4.2
HSD9@3	1406	1164	82	0.828	0.32593	1.97	0.0448	1.50	0.05279	1.28	282.4	4.2
HSD9@4	210	158	12	0.754	0.32415	2.74	0.0453	1.50	0.05195	2.29	285.3	4.2
HSD9@5	770	315	41	0.409	0.32032	1.93	0.0449	1.50	0.05177	1.21	283.0	4.2
HSD9@6	973	642	55	0.660	0.32374	1.87	0.0449	1.50	0.05233	1.12	282.9	4.2
HSD9@9	366	131	18	0.356	0.30593	2.35	0.0433	1.52	0.05125	1.80	273.2	4.1
HSD9@10	463	162	24	0.351	0.31157	2.01	0.0441	1.51	0.05126	1.33	278.1	4.1
HSD9@11	215	121	11	0.562	0.31163	2.44	0.0420	1.52	0.05381	1.92	265.2	3.9
HSD9@14	1185	485	62	0.410	0.31885	1.84	0.0447	1.51	0.05176	1.05	281.8	4.2
HSD9@15	275	96	14	0.350	0.31476	2.24	0.0441	1.51	0.05173	1.65	278.4	4.1
HSD9@16	1107	814	64	0.735	0.31730	1.74	0.0446	1.53	0.05161	0.84	281.2	4.2
HSD9@17	355	325	21	0.915	0.31647	2.63	0.0445	1.52	0.05159	2.14	280.6	4.2
HSD9@18	1184	867	67	0.732	0.31740	1.78	0.0442	1.51	0.05204	0.93	279.0	4.1
HSD9@19	1111	1152	68	1.037	0.32202	1.94	0.0446	1.51	0.05238	1.22	281.2	4.1
HSD9@20	684	515	40	0.753	0.32153	1.90	0.0449	1.50	0.05191	1.17	283.3	4.2

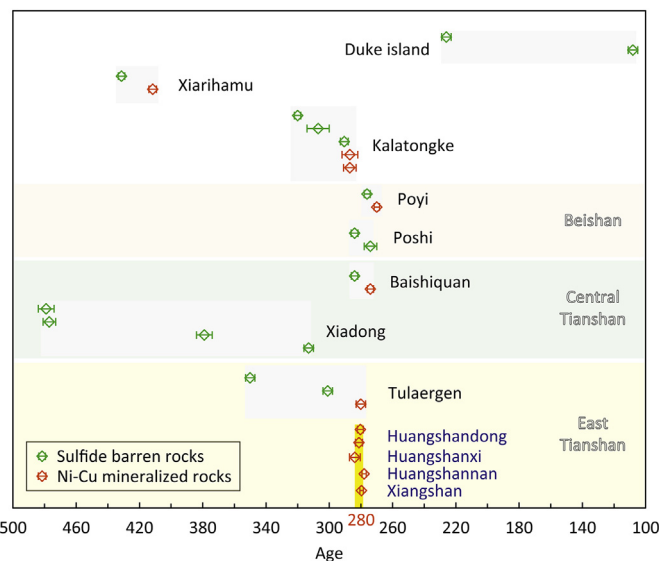


Fig. 3. Comparison of some protracted magmatism in convergent settings and the short-lived magmatism of the Huangshandong complex. All the age data collected in this study were produced from zircon U–Pb dating. Age sources: Duke Island (Gehrels et al., 1987; Saleby, 1992), Kalatongke (Qian et al., 2018), Poyi (Xue et al., 2016), Poshi (Qin et al., 2011), Tulaergen (Mao et al., 2018; San et al., 2010), Xiadong (Su et al., 2014), Baishiquan (Tang et al., in preparation), and Huangshandong (this study).

droplets could have been segregated from the magma and deposited along the conduit and/or at the sub-chamber. Subsequently, the occurrence of moderate olivine fractionation in the staging magma chamber produced the evolved magma (Phase III) entraining some sulfide droplets. Due to the density contrast, the early segregated sulfides in the staging chamber tend to accumulate with the cumulus olivine and lock within the pores of cumulus olivine. Such sulfide droplets, which are entrained in the magma, are most likely depleted in Ni (Ni tenor <1.7 wt%) as indicated by the low Ni contents (~600 ppm) in olivine from the Phase III rocks (Mao et al., 2015). However, the sulfide droplets equilibrium with the Phase III olivine are too depleted in Ni (Ni tenor <1.7 wt%) to form the ores in the current gabbro (Ni tenor of ~7, similar to the sulfides in Phase II) (Mao et al., 2015). Based on the similarity in sulfide composition between Phase II and Phase III rocks, it is proposed that the sulfides in the Phase III rocks were picked up from the conduit where some sulfides had been left by the Phase II magmas (Mao et al., 2015). The upward transportation of such evolved magma to a higher level produced the Phase III rocks (Fig. 5c). Finally, a relatively primitive magma injected into the staging chamber, driving the residual magma to less evolved magma. The ascent of such magma through the current location generated the Phase IV olivine websterite and lherzolite with disseminated sulfides (Fig. 5d).

Our interpretation of the magma evolution in a deep-seated magma chamber (Fig. 5) and previous findings indicate that transportation of sulfide droplets from a deep-seated magma chamber and then deposition in another location played a critical role in the formation of the

Table 2

Hafnium and O isotopic compositions in zircon from the four phases rocks in the Huangshandong complex.

Sample	$^{176}\text{Yb}/^{177}\text{Hf}$	2σ	$^{176}\text{Lu}/^{177}\text{Hf}$	2σ	$^{176}\text{Hf}/^{177}\text{Hf}$	2σ	$(^{176}\text{Hf}/^{177}\text{Hf})_i$	$\epsilon\text{Hf (t)}$	$\delta^{18}\text{O}$	1σ
									%	%
Phase I, olivine gabbro										
G2@1	0.022554	0.000326	0.000927	0.000008	0.282962	0.000030	0.282957	12.7	6.04	0.22
G2@2	0.023741	0.000058	0.000968	0.000002	0.282979	0.000027	0.282974	13.3	6.39	0.20
G2@3	0.020675	0.000142	0.000856	0.000006	0.282978	0.000025	0.282973	13.3	6.57	0.31
G2@4	0.022120	0.000064	0.000934	0.000001	0.282987	0.000025	0.282982	13.6	6.41	0.30
G2@5	0.014224	0.000099	0.000601	0.000004	0.282944	0.000025	0.282941	12.1	6.37	0.29
G2@7	0.033541	0.001568	0.001333	0.000058	0.283009	0.000024	0.283002	14.3	6.13	0.28
G2@8	0.017245	0.000317	0.000719	0.000011	0.282948	0.000027	0.282944	12.3	6.58	0.25
G2@9	0.022776	0.000127	0.000966	0.000003	0.282964	0.000025	0.282959	12.8	6.17	0.22
G2@10	0.027066	0.000044	0.001130	0.000002	0.282951	0.000024	0.282945	12.3	6.10	0.25
G2@11	0.018100	0.000264	0.000740	0.000011	0.282953	0.000030	0.282949	12.4	6.70	0.26
G2@12	0.021577	0.000080	0.000869	0.000003	0.282928	0.000024	0.282924	11.5	6.22	0.36
G2@13	0.019569	0.000120	0.000780	0.000007	0.282975	0.000026	0.282971	13.2	6.53	0.26
G2@14	0.020341	0.000176	0.000833	0.000006	0.282989	0.000024	0.282985	13.7	6.32	0.28
G2@15	0.018582	0.000166	0.000795	0.000006	0.282964	0.000027	0.282960	12.8	6.74	0.25
G2@16	0.021949	0.000254	0.000914	0.000009	0.282995	0.000024	0.282990	13.9	6.44	0.31
G2@17	0.057699	0.001125	0.002163	0.000036	0.282907	0.000026	0.282895	10.5	6.38	0.21
G2@18	0.026782	0.000085	0.001063	0.000002	0.282897	0.000028	0.282891	10.4	6.37	0.26
G2@19	0.023379	0.000161	0.001014	0.000006	0.282986	0.000026	0.282980	13.5	6.46	0.28
G2@20	0.037955	0.000949	0.001531	0.000035	0.283002	0.000029	0.282994	14.0	6.40	0.34
G2@21	0.023480	0.000268	0.000999	0.000010	0.283007	0.000026	0.283002	14.3	6.13	0.26
G2@22	0.038611	0.000507	0.001623	0.000025	0.283031	0.000033	0.283023	15.0	6.54	0.34
G2@23									6.53	0.28
G2@24									6.38	0.28
Phase II, olivine websterite										
DJ610-a-10-6@1	0.012368	0.000036	0.000481	0.000001	0.282988	0.000026	0.282986	13.7	6.35	0.25
DJ610-a-10-6@2	0.052101	0.000649	0.001987	0.000025	0.282974	0.000032	0.282963	12.9	6.39	0.28
DJ610-a-10-6@4	0.017602	0.000365	0.000715	0.000014	0.282989	0.000023	0.282985	13.7	6.42	0.20
DJ610-a-10-6@5	0.019361	0.000280	0.000787	0.000011	0.282973	0.000024	0.282968	13.1	6.24	0.31
DJ610-a-10-6@6	0.021655	0.000036	0.000966	0.000001	0.283002	0.000025	0.282997	14.1	6.13	0.22
DJ610-a-10-6@7	0.025181	0.000068	0.000981	0.000003	0.282964	0.000023	0.282958	12.8	6.34	0.31
DJ610-a-10-6@8	0.045487	0.000221	0.001669	0.000006	0.282964	0.000024	0.282955	12.7	6.28	0.15
DJ610-a-10-6@9	0.010994	0.000075	0.000473	0.000003	0.282983	0.000025	0.282981	13.6	6.73	0.30
DJ610-a-10-6@10	0.020796	0.000064	0.000959	0.000002	0.283017	0.000030	0.283012	14.7	6.31	0.18
DJ610-a-10-6@11	0.018727	0.000702	0.000813	0.000028	0.283027	0.000030	0.283023	15.1	6.01	0.32
DJ610-a-10-6@14	0.050437	0.000152	0.001975	0.000007	0.283031	0.000030	0.283020	15.0	6.57	0.30
DJ610-a-10-6@15	0.024046	0.000165	0.001002	0.000007	0.283010	0.000032	0.283005	14.4	6.33	0.37
DJ610-a-10-6@16	0.011003	0.000047	0.000454	0.000002	0.283004	0.000027	0.283002	14.3	6.54	0.30
DJ610-a-10-6@17	0.03169	0.000587	0.001386	0.000022	0.282948	0.000027	0.282941	12.2	6.20	0.25
DJ610-a-10-6@18	0.012790	0.000144	0.000539	0.000005	0.282987	0.000023	0.282984	13.7	6.51	0.18
DJ610-a-10-6@19	0.025439	0.000146	0.001035	0.000006	0.282985	0.000025	0.282979	13.5	6.78	0.15
DJ610-a-10-6@20	0.013628	0.000034	0.000566	0.000001	0.282939	0.000034	0.282936	12.0	6.12	0.20
DJ610-a-10-6@22	0.033905	0.000181	0.001402	0.000006	0.282921	0.000029	0.282913	11.2	6.08	0.32
DJ610-a-10-6@23									6.50	0.30
DJ610-a-10-6@24									5.97	0.22
Phase III, gabbronorite										
DJ7007-1@1	0.037817	0.000641	0.001593	0.000027	0.282932	0.000028	0.282924	11.5	6.57	0.27
DJ7007-1@2	0.029948	0.001551	0.001269	0.000062	0.282948	0.000028	0.282941	12.2	6.36	0.19
DJ7007-1@3	0.032341	0.000146	0.001399	0.000005	0.282939	0.000026	0.282932	11.8	6.19	0.34
DJ7007-1@4	0.067995	0.001279	0.002645	0.000044	0.282953	0.000026	0.282939	12.1	6.34	0.32
DJ7007-1@5	0.042793	0.001612	0.001803	0.000065	0.283010	0.000026	0.283000	14.2	6.31	0.26
DJ7007-1@6	0.058217	0.001111	0.002292	0.000043	0.282951	0.000026	0.282939	12.1	6.39	0.15
DJ7007-1@7	0.045130	0.000376	0.001871	0.000011	0.283005	0.000026	0.282996	14.1	6.57	0.32
DJ7007-1@9	0.075325	0.000325	0.003091	0.000016	0.282997	0.000031	0.282980	13.5	6.36	0.26
DJ7007-1@10	0.016806	0.000446	0.000696	0.000019	0.282924	0.000029	0.282921	11.4	6.33	0.33
DJ7007-1@11	0.038674	0.000227	0.001642	0.000007	0.282915	0.000032	0.282907	10.9	6.66	0.30
DJ7007-1@12	0.075542	0.000208	0.002892	0.000010	0.283046	0.000028	0.283031	15.3	6.16	0.30
DJ7007-1@13	0.058328	0.000742	0.002335	0.000027	0.283010	0.000030	0.282997	14.1	6.08	0.26
DJ7007-1@14	0.046567	0.000503	0.001935	0.000017	0.282949	0.000028	0.282939	12.1	6.39	0.24
DJ7007-1@15	0.066980	0.000387	0.002633	0.000022	0.283076	0.000029	0.283062	16.4	6.25	0.39
DJ7007-1@16	0.045183	0.001332	0.001872	0.000050	0.282941	0.000025	0.282931	11.8	6.54	0.27
DJ7007-1@17	0.051936	0.000269	0.002132	0.000012	0.283027	0.000025	0.283016	14.8	6.43	0.35
DJ7007-1@18	0.037706	0.001560	0.001600	0.000060	0.282911	0.000029	0.282902	10.8	6.60	0.34
DJ7007-1@19	0.052400	0.000516	0.002135	0.000019	0.282973	0.000025	0.282962	12.9	6.32	0.29
DJ7007-1@20	0.056006	0.000291	0.002312	0.000011	0.282947	0.000029	0.282935	11.9	6.17	0.27
DJ7007-1@21									6.41	0.33
DJ7007-1@22									6.47	0.28
Phase IV, olivine websterite										
HSD9@1	0.036653	0.000473	0.001648	0.000021	0.282923	0.000028	0.282914	11.2	6.47	0.34
HSD9@2	0.061989	0.000291	0.002618	0.000013	0.282904	0.000024	0.282890	10.4	6.45	0.23
HSD9@3	0.026960	0.001390	0.001209	0.000060	0.282942	0.000026	0.282936	12.0	6.74	0.16

Table 2 (continued)

Sample	$^{176}\text{Yb}/^{177}\text{Hf}$	2σ	$^{176}\text{Lu}/^{177}\text{Hf}$	2σ	$^{176}\text{Hf}/^{177}\text{Hf}$	2σ	$(^{176}\text{Hf}/^{177}\text{Hf})_i$	$\epsilon\text{Hf(t)}$	$\delta^{18}\text{O}$	1σ
									%	%
HSD9@4	0.052660	0.000273	0.002320	0.000011	0.282984	0.000026	0.282972	13.2	6.38	0.26
HSD9@5	0.049820	0.000748	0.002169	0.000031	0.282977	0.000026	0.282965	13.0	6.33	0.32
HSD9@6	0.042966	0.000638	0.001890	0.000025	0.282931	0.000022	0.282921	11.4	6.47	0.23
HSD9@7	0.028214	0.000653	0.001287	0.000030	0.282947	0.000022	0.282940	12.1	6.25	0.28
HSD9@8	0.052672	0.000801	0.002236	0.000033	0.282904	0.000024	0.282892	10.4	6.29	0.28
HSD9@10	0.040410	0.000954	0.001834	0.000041	0.282967	0.000025	0.282958	12.7	6.13	0.31
HSD9@11	0.021676	0.000939	0.001013	0.000043	0.282929	0.000024	0.282924	11.6	6.19	0.22
HSD9@12	0.031362	0.000563	0.001434	0.000023	0.282993	0.000026	0.282985	13.7	6.25	0.25
HSD9@13	0.042687	0.000213	0.001886	0.000009	0.282977	0.000025	0.282967	13.1	6.24	0.37
HSD9@14	0.025045	0.001017	0.001149	0.000044	0.282962	0.000022	0.282956	12.7	6.49	0.36
HSD9@15	0.026867	0.000893	0.001272	0.000040	0.282965	0.000022	0.282959	12.8	6.30	0.46
HSD9@16	0.017637	0.000601	0.000803	0.000025	0.282970	0.000022	0.282966	13.0	6.15	0.31
HSD9@18	0.045123	0.001750	0.001979	0.000069	0.282944	0.000023	0.282934	11.9	6.23	0.26
HSD9@19	0.032775	0.000785	0.001485	0.000034	0.282921	0.000023	0.282913	11.2	6.24	0.38
HSD9@20	0.043491	0.000324	0.001887	0.000012	0.282920	0.000025	0.282910	11.1	5.96	0.27
HSD9@21									6.23	0.25
HSD9@22									6.40	0.28
HSD9@23									6.35	0.25
t = 281										

Huangshandong deposit. The key ore-forming processes of the Huangshandong deposit could be summarized as 1) sulfide saturation took place in the deep-seated magma chamber forming sulfide droplets entrained magma which contains a small proportion of sulfide, probably in an open system; 2) continuous flow through of the sulfide-entrained magma and deposition of the droplets at particular locations. The former process is consistent with “the deep-seated magmatic liquation-injection mineralization” model proposed by Tang (1996), whereas the latter is essentially different from Tang’s model which requires emplacement of extremely Ni-rich magma (ore-grade) from the deep-seated magma chamber.

4.2. Magmatic Ni–Cu mineralization via short-time late-stage magmatism

The long evolutionary duration of small intrusions in a convergent setting is shown in Fig. 3. For instance, the intrusions in the Kalatongke

area formed from magmatism have ages varying from 320 to 287 Ma (Qian et al., 2018), whereas the Poyi complex formed from magmatism have ages ranging from 276 to 270 Ma (Xue et al., 2016). The Poshi complex comprises rocks that are 274 and 284 Ma in age (Jiang et al., 2006; Qin et al., 2011), whilst the Tulaergen complex is comprised of rocks that are 350 to 280 Ma in age (Mao et al., 2018; San et al., 2010). Similarly, the Xirihamu intrusions in the Kunlun Orogenic Belt comprise rocks that formed at 431–411 Ma (Li et al., 2015). These age differences are significantly larger than the analytical error (~2 Ma). The longest evolutionary duration is seen in the subduction-related Alaskan-type intrusion (Xiadong and Duke Island intrusions), which could have lasted as long as >100 Ma (Fig. 3) (Gehrels et al., 1987; Saleby, 1992; Su et al., 2014, 2017). Such long-term magma emplacements in the same locations could have been the result of long-term magmatism occurring during subduction and post-subduction processes, which are most likely associated with multiple partial melting of the mantle (Gao and Zhou, 2013b; Su et al., 2014).

In contrast, the four magma pulses of the Huangshandong complex were associated with short-term magmatism, which cannot be distinguished by SIMS dating (precision of 1–2 Ma). Furthermore, the SIMS U–Pb age of the intrusions in the Huangshan district (Huangshandong, Huangshanxi, Huangshannan, and Xiangshan intrusions) illustrate a uniform age of ~280 Ma (Fig. 3), suggesting a short duration of Ni–Cu mineralization in this area. Thus, it is possible that the large volume magmatism over a short time was related to a ~280 Ma mantle plume (Qin et al., 2011; Su et al., 2011; Tang et al., 2013), according to the extensive distribution of contemporaneous Ni–Cu mineralized mafic-ultramafic intrusions in the East Tianshan. Notably, even for intrusions that consist of rocks of large age variation in the East Tianshan and other convergent settings, the Ni–Cu mineralization was strongly related to the relatively late stage magmatism (Fig. 3). This may be explained by the upwelling of a large volume of the asthenosphere to the mantle wedge at the late stage of subduction and post-collisional period of orogenic belt, as illustrated by the depleted Sr–Nd–Hf isotopic values of the CAOB Ni–Cu mineralized intrusions (Deng et al., 2015; Li et al., 2015; Su et al., 2011; Sun et al., 2013; Wei et al., 2013). The most significant indication of such finding is that the basaltic magmatism occurring at the late stage of subduction and/or post-collisional period of the orogenic process in convergent settings may have significant potential to produce economic Ni–Cu mineralization, which most likely took place over a short time.

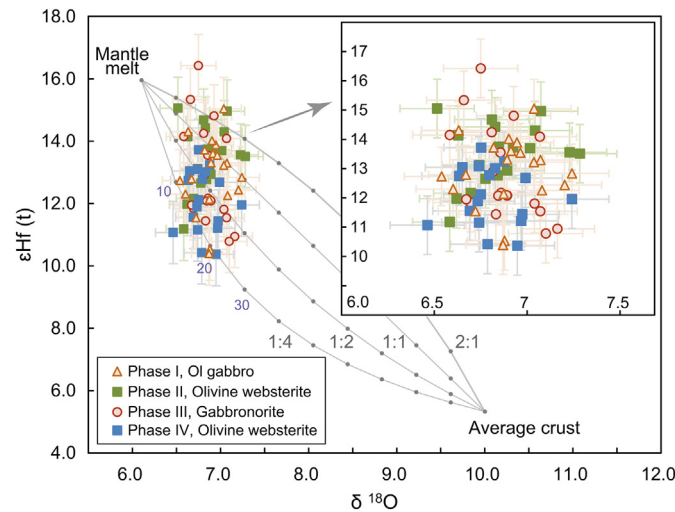


Fig. 4. Plots of the $\epsilon\text{Hf(t)}$ versus $\delta^{18}\text{O}$ values in the melt of the four phases of rocks from the Huangshandong complex, suggesting a 15–20% addition of crustal materials. The Hf and O isotopic values in the melt were calculated from the zircon composition. The modeling lines represent mixing between the average crust and the mantle melt, the numbers beside the line represent the ratio of Hf content in mantle melt to those in the average crust. The identical Hf–O isotopic values indicate that the four phases of magma may have been derived from the same magma chamber at depth.

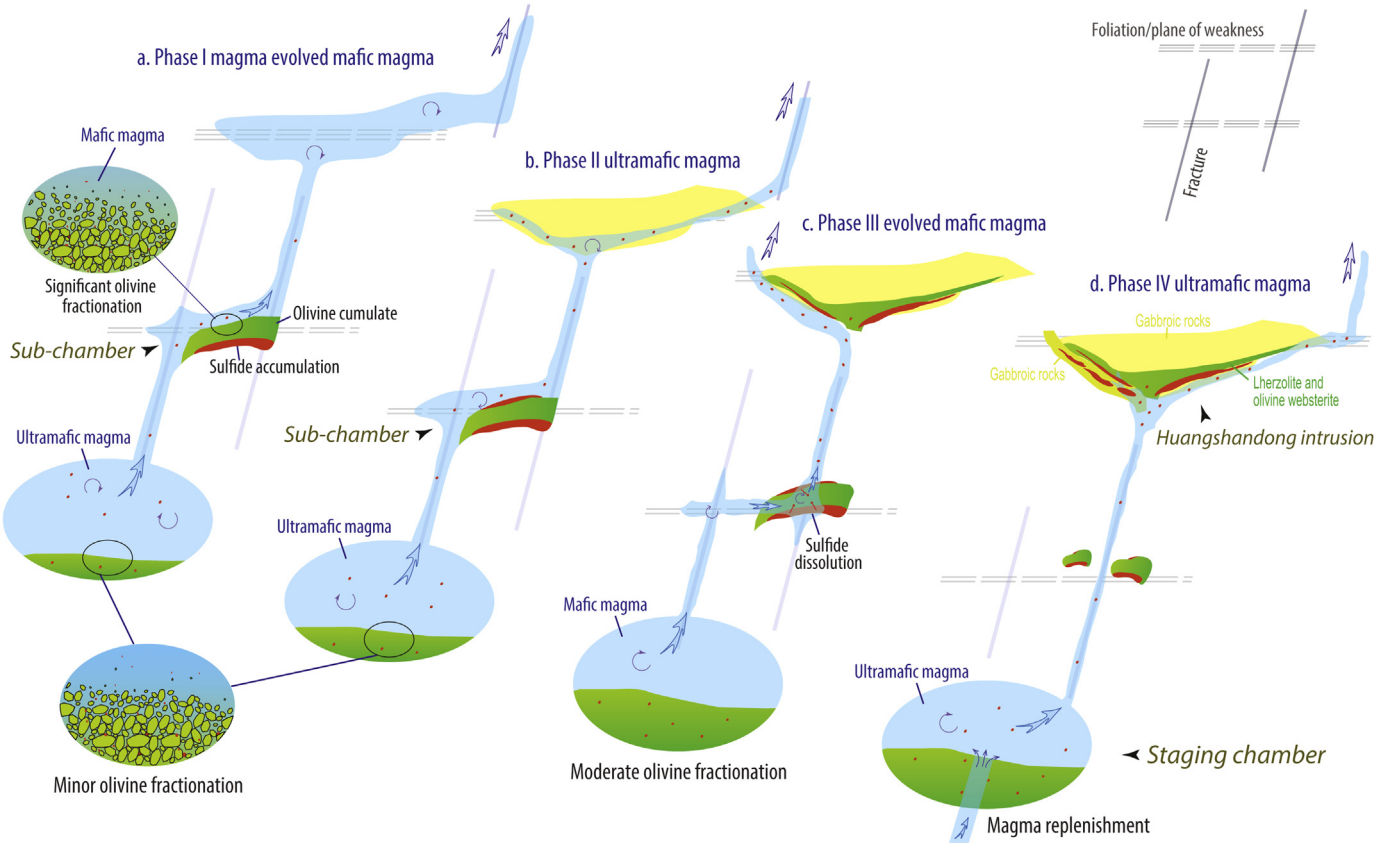


Fig. 5. Schematic illustration of the emplacement process of the Huangshandong complex, which shows the hypothetical magma evolution in the deep-seated magma chamber. See the text for explanations.

5. Conclusions

1. The four magma pulses of the Huangshandong deposit crystallized at ~280 Ma, showing that the Huangshandong complex formed over a short time.
2. The slightly elevated O isotopic values and enriched Hf isotopic values of zircon grains from different rock units could have resulted from 15 to 20% crustal material contamination.
3. The similar age and identical Hf–O isotopes suggest that the four magma pulses may have been originated from the same staging chamber, in which olivine fractionation and replenishment of relatively primitive magmas were two important factors that controlled the magma evolution.
4. Generally, the Ni–Cu mineralization, formed by late-stage magmatism in convergent settings, most likely took place within a short period.

Acknowledgments

This study was funded by grants from the National Key Research and Development Program of China (2017YFC0601204) and the Natural Science Foundation of China (41502095, 41872094). Guan-Liang Ren, Xue-Jun Yan, Jun-Hui Xie, and Li-Jie Kou from Yakesi Resource Development Ltd. are thanked for their guidance and help in the field. Shengchao Xue, Xian-Hua Li, Qiu-Li Li, Hong-Xia Ma and Yue-Heng Yang from the IGGCAS are acknowledged for their assistance with the laboratory work. Patrick Asamoah Sakyi polished English writing of this manuscript. Valuable comments from two anonymous reviews improved the manuscript. We thank Xian-Hua Li for his helpful suggestions and efficient editorial handling.

References

- Cawthorn, R.G., Walraven, F., 1998. Emplacement and crystallization time for the bushveld complex. *J. Petrol.* 39, 1669–1687.
- Deng, Y.-F., Song, X.-Y., Chen, L.-M., Zhou, T., Pirajno, F., Yuan, F., Xie, W., Zhang, D., 2014. Geochemistry of the Huangshandong Ni–Cu deposit in northwestern China: implications for the formation of magmatic sulfide mineralization in orogenic belts. *Ore Geol. Rev.* 56, 181–198.
- Deng, Y.-F., Song, X.-Y., Hollings, P., Zhou, T., Yuan, F., Chen, L.-M., Zhang, D., 2015. Role of asthenosphere and lithosphere in the genesis of the early Permian Huangshan mafic–ultramafic intrusion in the Northern Tianshan, NW China. *Lithos* 227, 241–254.
- Eiler, J.M., Crawford, A., Elliott, T., Farley, K.A., Valley, J.W., Stolper, E.M., 2000. Oxygen isotope geochemistry of oceanic-arc lavas. *J. Petrol.* 41, 229–256.
- Gao, J.-F., Zhou, M.-F., 2013a. Generation and evolution of siliceous high magnesium basaltic magmas in the formation of the Permian Huangshandong intrusion (Xinjiang, NW China). *Lithos* 162, 128–139.
- Gao, J.-F., Zhou, M.-F., 2013b. Magma mixing in the genesis of the Kalatongke dioritic intrusion: implications for the tectonic switch from subduction to post-collision, Chinese Altay, NW China. *Lithos* 162, 236–250.
- Gehrels, G.E., Saleby, J.B., Berg, H.C., 1987. Geology of Annette, Gravina, and Duke islands, southeastern Alaska. *Can. J. Earth Sci.* 24, 866–881.
- Han, B.F., Ji, J.Q., Song, B., Chen, L.H., Li, Z., 2004. SHRIMP zircon U–Pb ages of kalatongke no. 1 and Huangshandong Cu–Ni-bearing mafic-ultramafic complexes, North Xinjiang, and geological implications. *Chin. Sci. Bull.* 49, 2424–2429.
- Jiang, C., Cheng, S., Ye, S., Xia, M., Jiang, H., Dai, Y., 2006. Lithogeochemistry and petrogenesis of Zhongposhanbei mafic rock body, at Beishan region, Xinjiang. *Acta Petrol. Sin.* 22, 115–126.
- Li, X.H., Long, W.G., Li, Q.L., Liu, Y., Zheng, Y.F., Yang, Y.H., Chamberlain, K.R., Wan, D.F., Guo, C.H., Wang, X.C., Tao, H., 2010. Penglai zircon Megacrysts: a potential new working reference material for microbeam determination of Hf–O isotopes and U–Pb age. *Geostand. Geanalytical Res.* 34, 117–134.
- Li, C., Zhang, Z., Li, W., Wang, Y., Sun, T., Ripley, E.M., 2015. Geochronology, petrology and Hf–S isotope geochemistry of the newly-discovered Xiarihamu magmatic Ni–Cu sulfide deposit in the Qinghai–Tibet plateau, western China. *Lithos* 216–217, 224–240.
- Lightfoot, P.C., Evans-Lamswood, D., 2015. Structural controls on the primary distribution of mafic–ultramafic intrusions containing Ni–Cu–Co–(PGE) sulfide mineralization in the roots of large igneous provinces. *Ore Geol. Rev.* 64, 354–386.
- Mao, Y.-J., Qin, K.-Z., Li, C., Tang, D.-M., 2015. A modified genetic model for the Huangshandong magmatic sulfide deposit in the Central Asian Orogenic Belt, Xinjiang, western China. *Miner. Deposita* 50, 65–82.

- Mao, Y.-J., Qin, K.-Z., Tang, D.-M., Feng, H.-Y., Xue, S.-C., 2016. Crustal contamination and sulfide immiscibility history of the Permian Huangshannan magmatic Ni-Cu sulfide deposit, East Tianshan, NW China. *J. Asian Earth Sci.* 129, 22–37.
- Mao, Y.-J., Qin, K.-Z., Barnes, S.J., Iacono-Marziano, G., Ferrainac, C., Verrall, M., Tang, D., Xue, S., 2018. A revised oxygen barometry in sulfide-saturated magmas and application to the Permian magmatic Ni-Cu deposits in the southern Central Asian Orogenic Belt. *Miner. Deposita* 53, 731–755.
- Qian, Z., Duan, J., Li, C., Xu, G., Feng, Y., Ren, M., 2018. Paleozoic mafic-intermediate intrusions (320–287 Ma) in the Kalatongke area, southern Altai, NW China: Products of protracted magmatism in a convergent tectonic setting. *J. Asian Earth Sci.* 159, 294–307.
- Qin, K.-Z., Su, B.-X., Sakyi, P.A., Tang, D.M., Li, X.H., Sun, H., Xiao, Q.H., Liu, P.P., 2011. Sims zircon U-Pb geochronology and Sr-Nd isotopes of Ni-Cu-bearing mafic-ultramafic intrusions in eastern tianshan and Beishan in correlation with flood basalts in Tarim basin (NW China): constraints on a Ca. 280 Ma mantle plume. *Am. J. Sci.* 311, 237–260.
- Saleeby, J.B., 1992. Age and tectonic setting of the Duke Island ultramafic intrusion, southeast Alaska. *Can. J. Earth Sci.* 29, 506–522.
- San, J.Z., Qin, K.Z., Tang, Z.L., Tang, D.M., Su, B.X., Sun, H., Xiao, Q.H., Liu, P.P., 2010. Precise zircon U-Pb age dating of two mafic-ultramafic complexes at Tulargen large cu-Ni district and its geological implications. *Acta Petrol. Sin.* 26, 3027–3035.
- Scoates, J.S., Friedman, R.M., 2008. Precise age of the platinumiferous Merensky reef, bushveld complex, South Africa, by the U-Pb zircon chemical abrasion ID-TIMS technique. *Econ. Geol.* 103, 465–471.
- Song, X.Y., Chen, L.M., Deng, Y.F., Xie, W., 2013. Syncollisional tholeiitic magmatism induced by asthenosphere upwelling owing to slab detachment at the southern margin of the central Asian Orogenic Belt. *J. Geol. Soc.* 170, 941–950.
- Stacey, J.S., Kramers, J.D., 1975. Approximation of terrestrial lead isotope evolution by a two-stage model. *Earth Planet. Sci. Lett.* 26, 207–221.
- Su, B.-X., Qin, K.-Z., Sakyi, P.A., Li, X.-H., Yang, Y.-H., Sun, H., Tang, D.-M., Liu, P.-P., Xiao, Q.-H., Malaviarachchi, S.P.K., 2011. U-Pb ages and Hf-O isotopes of zircons from late Paleozoic mafic-ultramafic units in the southern Central Asian Orogenic Belt: tectonic implications and evidence for an early-Permian mantle plume. *Gondwana Res.* 20, 516–531.
- Su, B.-X., Qin, K.-Z., Zhou, M.-F., Sakyi, P.A., Thakurta, J., Tang, D.-M., Liu, P.-P., Xiao, Q.-H., Sun, H., 2014. Petrological, geochemical and geochronological constraints on the origin of the Xiadong Ural-Alaskan type complex in NW China and tectonic implication for the evolution of southern central Asian Orogenic Belt. *Lithos* 200–201, 226–240.
- Su, B.X., Hu, Y., Teng, F.Z., Qin, K.Z., Yang, B., Sakyi, P.A., Tang, D.M., 2017. Chromite-induced magnesium isotope fractionation during mafic magma differentiation. *Sci. Bull.* 62, 1538–1546.
- Sun, T., Qian, Z.Z., Deng, Y.F., Li, C.S., Song, X.Y., Tang, Q.Y., 2013. PGE and isotope (Hf-Sr-Nd-Pb) constraints on the origin of the Huangshandong magmatic Ni-Cu sulfide deposit in the central Asian Orogenic Belt, northwestern China. *Econ. Geol.* 108, 1849–1864.
- Tang, Z., 1996. The main mineralization mechanism of magma sulfide deposits in China [J]. *Acta Geol. Sin.* 3, 237–243.
- Tang, D., Qin, K., Su, B., Sakyi, P.A., Liu, Y., Mao, Q., Santosh, M., Ma, Y., 2013. Magma source and tectonics of the Xiangshanzhong mafic-ultramafic intrusion in the central Asian Orogenic Belt, NW China, traced from geochemical and isotopic signatures. *Lithos* 170–171, 144–163.
- Valley, J.W., Lackey, J.S., Cavosie, A.J., Clechenko, C.C., Spicuzza, M.J., Basei, M.A.S., Bindeman, I.N., Ferreira, V.P., Sial, A.N., King, E.M., Peck, W.H., Sinha, A.K., Wei, C.S., 2005. 4.4 billion years of crustal maturation: oxygen isotope ratios of magmatic zircon. *Contrib. Mineral. Petrol.* 150, 561–580.
- Vervoort, J.D., Blachert-Toft, J., 1999. Evolution of the depleted mantle: Hf isotope evidence from juvenile rocks through time. *Geochim. Cosmochim. Acta* 63, 533–556.
- Wang, R.M., Liu, D.Q., Yin, D.T., 1987. The conditions of controlling metallogeny of cu-Ni sulfide ore deposits and the orientation of finding ore Hami, Xinjiang, China. *J. Mineral. Petrol.* 7, 1–152.
- Wang, T., Li, W., Li, J., Hong, D., Tong, Y., Li, S., 2008. Increase of juvenile mantle-derived composition from syn-orogenic to post-orogenic granites in the east part of the eastern Tianshan (China) and implications for continental vertical growth: Sr and Nd isotopic evidence. *Acta Petrol. Sin.* 24, 762–772.
- Wei, B., Wang, C.Y., Li, C., Sun, Y., 2013. Origin of PGE-depleted Ni-Cu sulfide mineralization in the Triassic Hongqiling no. 7 Orthopyroxenite intrusion, Central Asian Orogenic Belt, northeastern China. *Econ. Geol.* 108, 1813–1831.
- Xiao, W.J., Zhang, L.C., Qin, K.Z., Sun, S., Li, J.L., 2004. Paleozoic accretionary and collisional tectonics of the eastern Tianshan (China): implications for the continental growth of Central Asia. *Am. J. Sci.* 304, 370–395.
- Xue, S., Qin, K., Li, C., Tang, D., Mao, Y., Qi, L., Ripley, E.M., 2016. Geochronological, petrological, and geochemical constraints on Ni-Cu sulfide mineralization in the Poyi ultramafic-Troctolitic intrusion in the northeast rim of the Tarim craton, western China. *Econ. Geol.* 111, 1465–1484.
- Zhou, M.F., Lesher, C.M., Yang, Z.X., Li, J.W., Sun, M., 2004. Geochemistry and petrogenesis of 270 ma Ni-Cu-(PGE) sulfide-bearing mafic intrusions in the Huangshan district, Eastern Xinjiang, Northwest China: implications for the tectonic evolution of the Central Asian orogenic belt. *Chemical Geology* 209, 233–257.